

Fatigue limits in noncyclic loading of ceramics with crack-resistance curves

S. LATHABAI*, BRIAN R. LAWN

Ceramics Division, National Institute of Standards and Technology, Gaithersburg, Maryland 20899, USA

Fatigue properties in the noncyclic loading of ceramics with R -curves are studied. Particular attention is directed to the potential role of R -curves in the enhancement of fatigue limits. A numerical algorithm for solving the appropriate differential equations of rate-dependent failure is developed. Our formalism specifically incorporates a crack-size dependent toughness function, based on grain-localized interfacial bridging, and a hyperbolic-sine velocity function, representative of a fundamental activation process. In a case study, dynamic fatigue (constant stressing rate) and static fatigue (constant applied stress) data for a coarse-grained alumina with a pronounced R -curve are analysed. With foreknowledge of the toughness parameters, the intrinsic crack-tip velocity function is deconvoluted. This intrinsic function is distinguished from the usual "apparent", or "shielded", (and demonstrably nonunique) function determined directly from the external load. It is confirmed that the R -curve, by virtue of its stabilizing influence on the crack growth, significantly enhances the fatigue limit, and confers the quality of "flaw tolerance" on fatigue lifetimes.

1. Introduction

Brittle solids are susceptible to delayed failure induced by "slow" growth of flaws to critical dimensions [1]. In the ceramics community, such delayed failure is referred to as "fatigue", even for noncyclic loading conditions, e.g. constant stress ("static" fatigue) or constant stressing rate ("dynamic" fatigue). Experimental data are usually represented as linear plots on appropriate (logarithmic-coordinate) fatigue diagrams (applied stress against failure time, or failure stress against stressing rate), the slopes of which determine a fatigue "susceptibility". Embodied in most analytical treatments of these plots are certain idealizations concerning the fracture mechanics, e.g. that the strength-controlling flaws are free of any residual driving forces and that the material has a single-valued toughness, such that the (inverse) susceptibility is directly identifiable with the exponent in a power-law crack velocity relation [2, 3]. Characteristic features of such treatments are: (i) an implied uniqueness of the crack velocity–mechanical energy release rate (v – G) function for a given material–environment system; (ii) a critical dependence of the ensuing lifetime characteristics on the initial flaw size.

An important shortcoming of the conventional log-linear analysis of time-to-failure behaviour in ceramics is the lack of provision for a fatigue limit. The existence of a bounding applied stress, σ_{lim} , say, below which a component effectively has infinite lifetime, is an attractive prospect in engineering design. Efforts to detect such lower bounds as deviations from linear response

in the long-lifetime domain of fatigue diagrams have been few, due partly to the notorious scatter in strength-related data and partly to self-imposed short-term restrictions on data accumulation, this despite a well established precedent for analogous fatigue limits in the metals literature [4]. A study by Cook [5] on sapphire, using indentation flaws to reduce the scatter and extend the range of constant stressing rate data, is one exception. That author attributes the observation of an asymptotic lower limit in the sapphire strength to a threshold in the underlying crack velocity function, i.e. to the existence of a zero velocity state at (positive) nonzero applied load. Cook used a power-law velocity function in stress intensity factor, K , with cutoff to describe this threshold; we shall assert that the velocity function is written more justifiably as a hyperbolic sine in $G - 2\gamma$, where γ is a thermodynamic surface energy. Direct measurements of rate-dependent crack growth in large-scale crack specimens of other brittle materials [6, 7] suggest that velocity thresholds, and thence fatigue limits, might be more prevalent in ceramics than previously suspected. In any event, it seems apparent that anything we could do to the material system to augment this threshold would surely stand to improve lifetime characteristics.

There is a way in which improvement of this kind might be achieved, and that is to make use of the crack-stabilizing effect of R -curve (or T -curve) behaviour, i.e. a systematically increasing crack resistance R (or, equivalently, toughness T), with extension [8]. R -curve behaviour arises because of the shielding of

*Guest Scientist: on leave from the Department of Materials Science and Engineering, Lehigh University, Bethlehem, Pennsylvania 18015, USA.

the crack by some microstructure-associated energy-dissipative process in the region immediately surrounding the tip. It is now appreciated that many nontransforming ceramics exhibit such behaviour [8–16]. It has been argued on qualitative grounds that the restraining influence of shielding should extend to rate-dependent crack growth [17], and there is some experimental evidence in support of this contention in zirconia material systems [18]. However, the possibility of using shielding to improve lower-limit strength levels does not seem to have attracted much attention in the literature.

In the present paper we explore this last possibility. As a case study, we examine a material with pronounced *R*-curve behaviour, a coarse-grained alumina of a kind that has been investigated extensively in inert-environment (equilibrium) indentation-strength studies [8, 11, 13, 15]. The *R*-curve behaviour in polycrystalline alumina is due to persistent grain-localized bridging at the interface behind the (intergranularly) propagating crack tip. In developing a fatigue formalism we proceed in a manner similar to that described in earlier indentation-flaw fatigue studies [19–23] for materials with single-valued toughnesses, but with proper refinements. Now, we incorporate specific information on the *R*-curve (evaluated from control, inert-environment indentation-strength tests [8] on the same material) into a general hyperbolic sine v - G function to establish a starting differential equation. A numerical algorithm is thereby set up to obtain life-time solutions for prescribed time-dependent applied load states (constant stressing rate, constant stress). The algorithm is used to fit dynamic and static fatigue data on our alumina, and thence to determine unknown parameters in the v - G function.

More general implications of the analysis are then discussed.

(i) We confirm that the *R*-curve, because of its stabilizing influence on the crack growth, strongly enhances the fatigue limit. Indeed, we argue that a fatigue limit may even be apparent in materials that exhibit no natural threshold in the v - G relation.

(ii) We stress that the calibrated crack velocity function is the intrinsic v - G_* relation for the material-environment system, i.e. the fundamental relation that expressly determines the crack-tip motion. This relation is to be distinguished from the “engineering” v - G_a relation that would normally be obtained by monitoring the external load on the system. It is suggested that the intrinsic velocity relation may not be readily obtained in traditional large-crack tests, because of a history-dependence of the shielding component in G . Consequently, contrary to conventional expectation, the apparent v - G_a relation will generally not be unique.

(iii) We show that the fatigue lifetimes are not strongly dependent on initial flaw size; the quality of flaw tolerance in the strength characteristics for materials with *R*-curves [24] extends to fatigue properties.

Finally, the versatility of the procedure is indicated; once the velocity equation is calibrated, the algorithm may be used for *a priori* predictions of the fatigue

response in other, potentially more complex (e.g. cyclic) loading modes.

2. Fracture mechanics

In this section we outline the theoretical basis for determining failure lifetimes for ceramics with threshold crack velocity functions and with rising *R*-curves. We focus specifically on nontransforming materials whose *R*-curve is attributable to crack-interface bridging, although it is emphasized that the logical procedure for the analysis will be the same for other crack resistance processes. We start by writing expressions for the crack-size dependence of the mechanical energy release rate, $G(c)$, or the stress intensity factor, $K(c)$, incorporating the microstructural features that account for the toughness variation. Then we combine these expressions with the crack velocity relation, $v(G)$, to introduce a criterion for rate-dependent extension. Given the time dependence of the applied stress, $\sigma_a(t)$, a differential equation for the crack growth evolution can be constructed. The aim of the exercise is to evaluate this differential equation to determine the failure time, i.e. the time to take the initial strength-controlling flaw to a critical dimension for unlimited unstable propagation. Our analysis will be directed to controlled indentation flaws, but we stress at the outset that the formulation in this section is applicable to all flaw types.

2.1. Crack driving force and the *R*-curve

Consider first the mechanical driving force acting on the crack tip. As we shall argue in the next subsection, it is useful to express this driving force ultimately as a mechanical energy release rate, G . For the special case of crack propagation in the absence of any environmental effects, the fundamental Griffith condition for crack extension is expressible in terms of the energy release rate, $G_*(c)$ at the crack tip

$$G_* = 2\gamma_0 \quad (\text{equilibrium}) \quad (1)$$

where γ_0 is the fracture surface energy in inert atmospheres. In specifying γ_0 it is important to identify the mode of fracture: for our case study in Section 3 below we shall be concerned primarily with a polycrystalline material that shows essentially intergranular fracture, so that γ_0 must ultimately be relatable to a grain-boundary energy.

To make full use of the superposability of linear stress fields it is convenient to formulate the problem in terms of stress intensity factor notation, K . Accordingly, we seek an expression for $K_*(c)$, the net K -field experienced at the crack tip, and convert to $G_*(c)$ using the plane-strain transformation relation

$$G_* = K_*^2/E' \quad (2)$$

where $E' = E/(1 - \nu^2)$, with E = Young's modulus and ν = Poisson's ratio [25]. The net stress intensity factor will generally be made up of three components

$$K_*(c) = K_a(c) + K_r(c) + K_\mu(c). \quad (3)$$

$K_a(c)$ is the familiar contribution from the externally applied loading system. In most traditional treatments this is the only component that is considered. $K_r(c)$ is

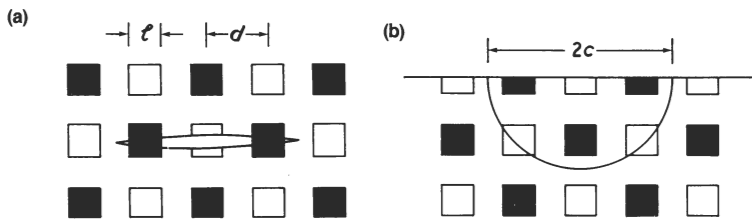


Figure 1 Growth of penny-like crack in bridging field; (a) side view, (b) projection view. (□) Out-of-plane bridging grains.

the contribution from any residual local stress fields associated with the formation of the crack. This is certainly an important term for the indentation flaws to be considered later, and may also be a significant factor in many naturally occurring flaw types. $K_\mu(c)$ is the contribution from the microstructural elements that are responsible for the R -curve. It is usually (not necessarily always) negative (closure field). The second and third terms in Equation 3 together effectively shield the crack tip field from the remote loading; it is only when these two terms are zero that we may revert to the simplistic identification of K_a with K_* that is implicit in most fatigue analyses for ceramic materials.

We need to specify the form of $K_\mu(c)$ for materials that exhibit R -curve behaviour by virtue of a crack-interface bridging mechanism. In the most recent analysis [8], the bridging restraint is modelled in terms of a “tail-dominated” stress-separation constitutive relation for interlocking grains on either side of the crack interface. The interlocking is assumed to be governed by internal matrix thermal expansion mismatch stresses, which “clamp” the bridging grains as the opposite crack walls separate. The bridges break by first debonding along the grain boundaries, and then sliding at these constrained boundaries until separation is complete. Coulomb friction at the grain-matrix interface during the latter pull-out stage accounts for the bulk of the energy dissipation responsible for the rising R -curve.

Suppose that our bridged crack system has essentially penny-like geometry, Fig. 1, as is pertinent to many flaw types and especially to indentation flaws. The solutions for the microstructural stress intensity factor may be derived in the pull-out-dominated limit of a linearly diminishing constitutive relation between closure stress, p , and (half) crack-opening displacement, u [8]

$$p(u) = p_M(1 - u/u_m), \quad (0 \leq u \leq u_m) \quad (4)$$

where p_M is the maximum resistance stress (at $u = 0$) and u_m is (half) the wall-wall displacement at grain-matrix disengagement (at $p = 0$). These last two parameters may be written more explicitly for rectangular, equiaxed microstructures as [8]

$$p_M = (4\mu\sigma_R u_m/l^2)(2d^2/l^2 - 1) \quad (5a)$$

$$u_m = \varepsilon_l l/2 \quad (5b)$$

where l is the mean grain diameter, d the bridge spacing, μ the coefficient of sliding friction, σ_R the magnitude of the internal stress, and ε_l the bridge rupture strain.

The solutions may be subdivided into three domains [8]: the precursor tensile zone, the bridging zone, and the saturation zone.

2.1.1. Precursor tensile zone ($c < d$)

Within this small-crack region no bridges are intersected, and the crack experiences only matrix tensile stresses $+\sigma_R$. There is a net driving force

$$K_\mu(c) = \psi\sigma_R c^{1/2} \quad (6)$$

where ψ is a geometry-dependent coefficient appropriate to penny cracks.

2.1.2. Bridging zone ($c \geq d$, $0 \leq u \leq u_m$)

The crack intersects bridges, and thereby has a positive component due to the persistent matrix tensile stresses and a countervailing component due to the integrated effect of the bridging tractions in Equation 4. In the approximation of “small shielding” (appropriate to ceramics with modest toughening [8]) we derive

$$K_\mu(c) = \psi\sigma_R c^{1/2}[1 - (1 - d^2/c^2)^{1/2}] - (E'p_M/K_*)[u_z(1 - u_z/2u_m)] \quad (7)$$

where u_z is (half) the crack-opening displacement at the stationary edge of the closure zone, i.e. location Z at $r = d$ in Fig. 2. The quantity $u_z(c)$ is determined separately from the Sneddon approximation for the crack profile equation at tip field K_*

$$u_z(c) = (\psi K_*/E')[((c^2 - d^2)/c)^{1/2}] \quad (8)$$

2.1.3. Saturation zone ($c \gg d$, $u \geq u_m$)

Ultimately, the first-intersected bridge at Z is pulled out and the bridging zone translates along with the crack. In this large-bridging domain only the second closure term in Equation 7 is significant, and this reduces to

$$K_\mu(c) = -E'p_M u_m/2K_* \quad (9)$$

We note that K_μ depends on K_* in Equations 7 to 9, so that Equation 3 becomes an implicit function for the crack-tip stress intensity factor.

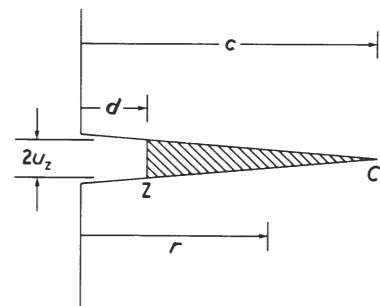


Figure 2 Coordinate system for crack-interface bridging. C , crack tip; Z , edge of the bridging zone.

2.2. Crack extension condition and the velocity function

Now consider the v - G relation that defines the fundamental kinetic condition for crack growth. We reiterate that the proper mechanical energy release rate in this relation is that experienced at the crack tip, i.e. G_* . We alluded in Section 1 to the shortcomings of the commonly used power-law function. The sole justification for retention of the empirical power-law function in traditional reliability formalisms has been the closed-form integrability of the ensuing fatigue lifetime differential equation [1–3]. However, with the introduction of the complex R -curve phenomenology into the $G_*(c)$ and $K_*(c)$ relations (Section 2.1), closed-form solutions are no longer feasible; there is thus nothing to be lost by introducing a physically based, if more complex, velocity function, in particular one that provides for a threshold.

Accordingly, we resort to a hyperbolic sine function, based on the underlying notion of stress-enhanced thermal activation over atomically localized energy barriers [5, 25–27]

$$v(G_*) = v_0 \sinh [(G_* - 2\gamma_1)/2\Gamma] \quad (2\gamma_1 \leq G_* \leq 2\gamma_0) \quad (10a)$$

$$v(G_*) = 0 \quad (2\gamma_1 > G_*) \quad (10b)$$

$$v(G_*) = v_T \quad (2\gamma_0 < G_*) \quad (10c)$$

where γ_1 is the fracture surface energy in the presence of the reactive environment (i.e. lowered from γ_0), v_0 and Γ are intercept and slope (susceptibility) parameters, and v_T is a terminal velocity ($\simeq 10^3$ msec⁻¹). Again, the value of γ_1 is that corresponding to intergranular fracture. The velocity function $v(G_*)$ is sketched in Fig. 3. Note the provision in Equation 10a for a threshold. The insistence that the velocity be zero at $G_* < 2\gamma_1$ in Equation 10b is consistent with the practical experience that cracks generally do not heal in polycrystalline materials. At $G_* > 2\gamma_0$ the crack is able to propagate even in the absence of a reactive environment (cf. Equation 1), and rapidly attains dynamic velocities. Within these two cut-off extremes the velocity closely approximates an exponential dependence on G_* .

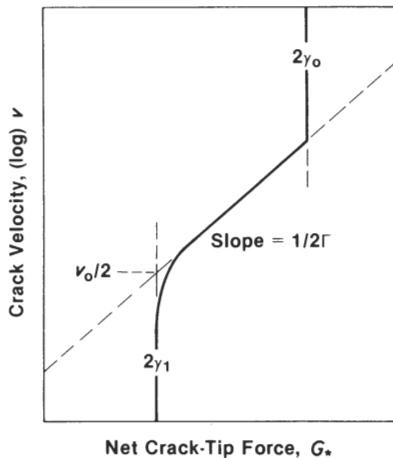


Figure 3 Schematic $v(G_*)$ function in Equation 10, plotted logarithmically on v axis and linearly on G_* axis.

2.3. Differential equation for “static” and “dynamic” fatigue of indentation flaws

Finally, we develop the formalism for crack systems in time-dependent applied stress fields, $\sigma_a = \sigma_a(t)$, as pertains to strength considerations. For uniform stresses we may immediately write

$$K_a(c) = \psi \sigma_a c^{1/2} \quad (11)$$

for the applied stress intensity factor in Equation 3. The applied stress states $\sigma_a(t)$ of specific interest to us here are those of so-called “static fatigue”

$$\sigma_a = \text{const.} \quad (12a)$$

and “dynamic fatigue”

$$\dot{\sigma}_a = \sigma_a/t = \text{const.} \quad (12b)$$

Also of specific interest here are indentation flaws. This flaw type is distinguished by a residual contact field [28]

$$K_r(c) = \chi P/c^{3/2} \quad (13)$$

with P the contact load and χ an elastic-plastic coefficient [15, 28].

Writing $v = dc/dt$, Equation 10 may be combined with Equations 2 to 9 and 11 to 13 into a differential equation for $c(t)$ at fixed load P and stress σ_a or stress rate $\dot{\sigma}_a$. This composite differential equation has to be solved for the time to grow the crack from an initial equilibrium state to final instability, i.e. the “time to failure”. Usually (but not always, see Section 4), the initial crack size, c_i , is calculated from Equations 2 to 9 by setting $G_*(c_i) = 2\gamma_1$ (zero velocity) at $K_a = 0$; likewise, the final crack size, c_f , is determined as the configuration $G_*(c_f) = 2\gamma_0$ (dynamic velocity) at which the system achieves uninterrupted propagation (see Section 3).

It is pointed out that Equations 11 to 13 are special cases, and that our formalism in Sections 2.1 and 2.2 is readily extendable to any general loading configuration, $K_a[\sigma_a(t)]$, and to any residual stress state for the strength-controlling flaw, $K_r(c)$.

2.4. Numerical algorithm for solution of fatigue differential equation

We have indicated that the general differential equation for kinetic crack growth in materials with R -curves has no closed-form solution. It is necessary to resort to numerical analysis. Consequently, a suitably expanded version of an earlier computer algorithm [19, 20] for determining static and dynamic fatigue times is employed. The algorithm increments c and t in Equation 10 in a Runge-Kutta stepwise integration procedure, readjusting $\sigma_a(t)$ (where necessary, e.g. dynamic fatigue), hence $G_*(c, t)$ (after iterative solution of implicit expression for K_* , Equation 3, see Section 2.1), at each step.

Special attention to the stepping procedure in this algorithm is in order, owing to the typically enormous range of crack velocities embraced in the evolution to failure; a fixed increment in time runs the very clear risk of stalling the evaluation in the regions of slow growth and, conversely, of blowing it up in the regions of fast growth. It is necessary to adopt a stepping

strategy that provides a reasonable compromise between accuracy and time of computation. Consequently, our algorithm incorporates computational elements that allow for automatic readjustment of the increments, according to the instantaneous velocity. One of these elements involves an inversion of the underlying differential equation, $dc/dt = v(c, t)$: at low velocities (i.e. relative to v_0 , see Fig. 2), the equation retains its normal form — time is incremented, and the corresponding crack step determined from $dc = v(c, t)dt$; conversely, at high velocities, we rewrite the equation as $dt/dc = 1/v(c, t)$ — now crack size is incremented, and the Runge–Kutta routine suitably modified to determine the time step $dt = dc/v(c, t)$.

Another critical element in our algorithm is a provision to allow for intermediate, “pop-in” instabilities in the crack evolution. Such pre-failure jump-arrest events are indeed characteristic of materials with *R*-curves [13, 14, 29]. Consequently, a routine for predetermining all the unstable crack sizes, by solving Equation 1 at $dG_*/dc > 0$ in conjunction with Equations 2 to 9, is used to ensure that the programme is not stopped before the final, true failure instability is attained.

Once the *R*-curve and crack velocity parameters are specified, we may predetermine the fatigue characteristics for a given material–environment system: static fatigue curves directly as the times to failure t_f at specified applied stresses σ_a ; dynamic fatigue curves as the fatigue strengths $\sigma_f = \dot{\sigma}_a t_f$ at specified stressing rates $\dot{\sigma}_a$.

3. Results

3.1. Experimental procedure

Let us now demonstrate the formalism by analysing indentation-strength data on a commercial polycrystalline alumina ceramic, nominally pure (<0.1% additive) with grain size $l \simeq 23\ \mu\text{m}$ (Vistal grade Al_2O_3 , Coors Ceramic Co., Golden, Colorado, USA). The material is ostensibly the same as used in preceding studies [8, 11, 13, 23], but was obtained from a new batch. The intergranular-fracture, crack–interface bridging mechanism considered in Section 2.1 has been identified in this material [13], and the associated *R*-curve characteristics documented [8]. Dynamic fatigue test results in water have also been reported [23]. However, to avoid possible discrepancies from batch-to-batch variations, we obtain an entirely fresh set of data here.

Accordingly, specimens were tested in the form of discs, approximately 22 mm diameter and 2 mm thick. Controlled Vickers indentation flaws were introduced at the centres of the prospective tensile faces of each specimen. The indentations were immediately covered with silicon oil, for inert strength tests, or with water, for fatigue tests. A biaxial loading fixture, with a flat circular punch of diameter 4 mm on three-point support of diameter 19 mm, was used to break the specimens, and the surface tensile stress, σ_a , computed from thin plate formulae [11]. For the determination of inert strengths ($\sigma_a = \sigma_m$), the contact loads covered a broad range ($P = 3$ to 300 N), and the breaks made

at fast stressing rates ($> 10^4\ \text{MPa sec}^{-1}$). For the fatigue tests, a single, intermediate load ($P = 30\ \text{N}$) was used. Dynamic fatigue strengths ($\sigma_a = \sigma_f$) were determined over several decades of constant stressing rates ($\dot{\sigma}_a = 10^{-3}$ to $10^{+4}\ \text{MPa sec}^{-1}$), using a piezo-electric load cell [23] to extend the tests as far as practicable into the short-duration region ($< 20\ \text{msec}$); static fatigue times to failure (t_f) were determined at prescribed applied stresses ($\sigma_a = \text{const.}$) (ramp time $< 6\ \text{sec}$).

In all tests the broken specimens were examined to verify the indentation site as the origin of failure. Exceptions were excluded from the data pool.

3.2. Inert strength data and the *R*-curve parameters

The inert strength data, $\sigma_m(P)$, are shown in Fig. 4. These strength data tend strongly away from the conventional $P^{-1/3}$ dependence for materials with a single-valued toughness, toward a plateau at low P . The plateau is a measure of the flaw tolerance associated with *R*-curve behaviour [8, 14, 15]. A bridging parameter adjustment routine, iterating on Equations 2 to 9 [8], is used to obtain the best-fit solid curve in this diagram. Assuming $E' = 413\ \text{GPa}$, $\psi = 1.24$ and $\chi = 0.018$ for the alumina [8], we obtain our fit with the following parameter values: $\gamma_0 = 5.6\ \text{J m}^{-2}$ (grain boundary), $\varepsilon_i = 0.120$, $\mu = 1.80$, $\sigma_R = 155\ \text{MPa}$ and $d = 35\ \mu\text{m}$. This set of parameters determines the *R*-curve. (These parameters are similar to those in determined [8], except that γ_0 is about 15% lower, suggesting that our new batch of material may have slightly weaker grain boundaries.)

It is instructive to insert Equations 3 to 9 into Equation 2, and thence to evaluate the critical function $G_*(c)$ corresponding to the inert strength data point at $P = 30\ \text{N}$, $\sigma_m = 220\ \text{MPa}$, in Fig. 4. This function is plotted as the upper curve in Fig. 5. We note the principal minimum at $G_* = 2\gamma_0$, representing the configuration at failure.

3.3. Fatigue data and the crack velocity parameters

The dynamic and static fatigue results for our alumina are plotted in Figs 6 and 7, respectively. There is a

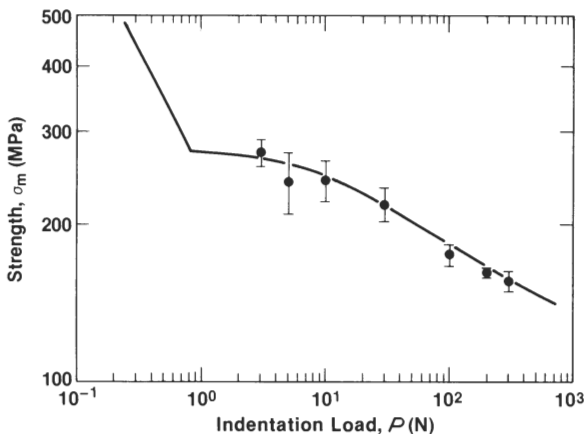


Figure 4 Inert strength–Vickers indentation load for polycrystalline alumina. Data points means and standard deviations (minimum ten specimens per point) in strength values. (—) Best fit obtained by adjusting parameters in bridging model.

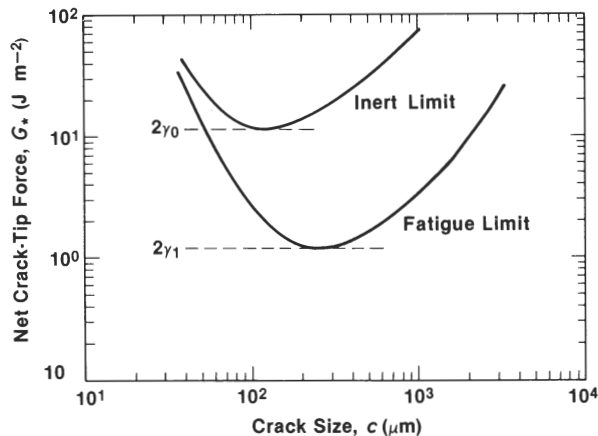


Figure 5 Plot of $G_*(c)$ for polycrystalline alumina, Vickers indentation flaw ($P = 30$ N) evaluated at constant $\sigma_a = \sigma_m = 220$ MPa (inert strength) and $\sigma_a = \sigma_{lim} = 130$ MPa (fatigue limit).

strong asymptotic tendency to a fatigue stress limit, σ_{lim} , in the long-time regions of both these plots. This tendency is most apparent in Fig. 7, reflecting a bias in the static testing methodology toward longer test durations; indeed, the data in Fig. 7 seem to lie almost exclusively in the fatigue-limit domain. At short times the data must saturate at the inert strength level; only in the dynamic data of Fig. 6 is the test duration short enough to indicate that this upper limit is, in fact, being approached.

The solid curves are best fits to the data, obtained using the R -curve parameters evaluated above (Section 3.1) and adjusting the crack velocity parameters in Equation 10. The procedure adopted for determining the velocity parameters involves two steps.

(i) The surface energy term, γ_1 , is evaluated from an estimate of the asymptotic fatigue limit, $\sigma_{lim} = 130$ MPa, in Figs 6 and 7. First we determine the critical function $G_*(c)$ appropriate to σ_{lim} , at indentation load $P = 30$ N, in exactly the same way as done previously for the inert strength σ_m , i.e. upper curve in Fig. 5. The new function is plotted as the lower curve in the same figure. Because the fatigue limit represents

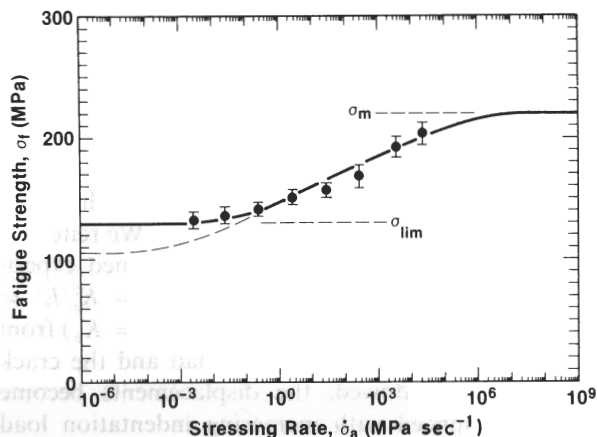


Figure 6 Dynamic fatigue plot for polycrystalline alumina in water, for Vickers indentations at $P = 30$ N. Data points means and standard deviations (minimum ten specimens per point) in strength values. σ_m is inert strength level, σ_{lim} is fatigue limit. (—) Best fit obtained by adjusting crack velocity parameters. (---) Equivalent fatigue response for material without crack velocity threshold (Section 4).

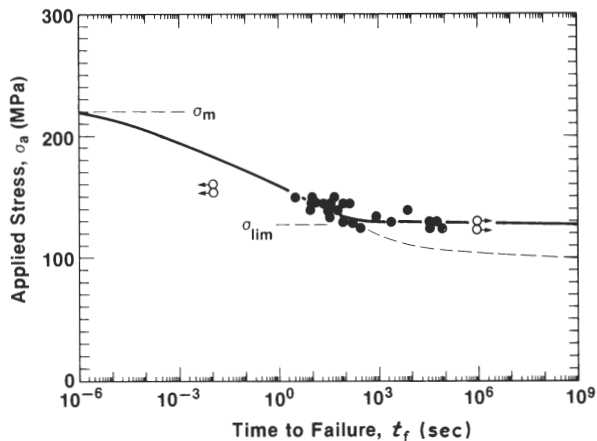


Figure 7 Static fatigue plot for polycrystalline alumina in water, for Vickers indentations at $P = 30$ N. Arrows at right designate interrupted tests, overlapping data for ten specimens. Arrows at left designate breakages during ramp loading to maximum applied stress, six specimens. Other data points are results of individual tests. σ_m is inert strength level, σ_{lim} is fatigue limit. (—) Best fit obtained by adjusting crack velocity parameters. (---) Equivalent fatigue response for material without velocity threshold.

the applied stress level below which the crack at some point in its evolution ceases all growth, the principal minimum in this lower curve necessarily defines the threshold state $G_*(c) = 2\gamma_1$ (i.e. $v = 0$ in Equation 10); hence from Fig. 5 we obtain $2\gamma_1 = 1.20$ J m $^{-2}$.

(ii) The parameters v_0 and Γ are now adjusted to give the best fit to the fatigue data points. The computer does this by selecting the combination of parameters that minimizes the variance between computed and measured data points at the experimental values of $\dot{\sigma}_a$ (dynamic fatigue) and σ_a (static fatigue). In making these adjustments, it is useful to recognize that v_0 reflects more strongly in the intercepts, Γ likewise more strongly in the slopes, of the fatigue plots. This procedure yields $v_0 = 7.0$ $\mu\text{m sec}^{-1}$, $\Gamma = 0.325$ J m $^{-2}$.

The intrinsic v - G_* function corresponding to the above parameter calibration is plotted in accordance with Equation 10 for our polycrystalline alumina in water as the solid curve in Fig. 8. Also included in

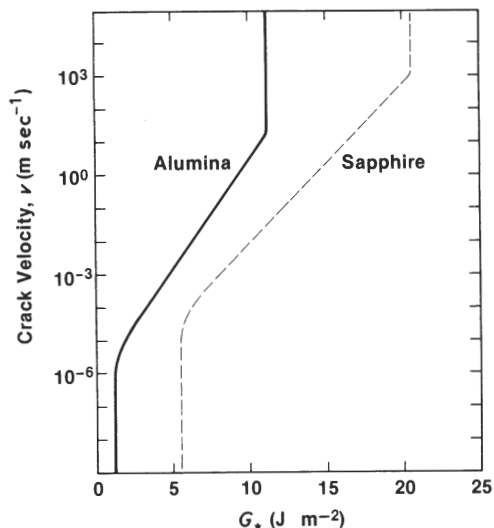


Figure 8 Plot of the intrinsic crack-tip velocity function, v - G_* , for polycrystalline alumina (—) in water, as determined from fits to fatigue data. Also included is corresponding function for single-crystal sapphire (---), using data from [23].

Fig. 8, as the dashed curve, is the analogous function for single-crystal sapphire in water, obtained by similarly deconvoluting fatigue data from [23] (requiring $K_\mu = 0$, but retaining the hyperbolic sine velocity function over the Cook cut-off power-law [5]). The curve for the polycrystalline material falls distinctly to the left of that for the single crystal. This is in accord with the fact that the fracture in the former is intergranular (cf. γ_0 value 5.6 J m^{-2} for our alumina with 11.0 J m^{-2} for sapphire, as reflected in the upper bounds to the two curves in Fig. 8).

4. Discussion

We have developed a formalism for studying (non-cyclic) fatigue limits in ceramic materials with *R*-curves. Introducing a microstructural closure stress intensity factor based on crack–interface bridging, and a threshold crack velocity function based essentially on activation kinetics, we have described a numerical algorithm that solves the ensuing fracture-mechanics differential equations for time-dependent failure. As an illustrative case study, dynamic and static fatigue limits for an alumina–water system with controlled (indentation) flaws have been quantified, and the intrinsic v – G_* curve thereby deconvoluted. Once the *R*-curve and velocity parameters have been calibrated from the fatigue data, the algorithm becomes a powerful tool for analysing and predicting various elements of the limiting failure conditions. We shall explore some of these elements in the discussion below.

It might be contended that the present study does little more than reinforce an existing suspicion that fatigue limits are possible in ceramics: all that is necessary is a threshold in the crack velocity function. The novel aspect here is our focus on the role of the *R*-curve; in particular, on how the additional crack stability afforded by the microstructural crack resistance may enhance these fatigue limits. Indeed, it can be argued that a fatigue limit may be achieved in an *R*-curve material without any velocity threshold at all. To demonstrate, we use our algorithm to compute the hypothetical fatigue responses for our alumina using the deconvoluted v – G_* function in Fig. 8, but with the threshold artificially reduced to $\gamma_1 = 0$ (i.e. as represented by the extrapolated, dashed line in Fig. 3, using a curve of the same Γ but with suitably adjusted intercept $v_0 = 1.0 \mu\text{m sec}^{-1}$ in Equation 10). The resulting modified fatigue relations are included as the dashed curves in Figs 6 and 7. We see that the prospective fatigue limit σ_{lim} is lowered, but not to zero. Physically, the existence of this limit is possible because the bridging closure term, $-K_\mu$ in Equation 3, can negate the applied loading term, $+K_a$ (plus K_r , where applicable), giving rise to a balance state $G_* = 0$ in Equation 2. In terms of the construction of Fig. 5, the requirement for attaining such a balance state is that the minimum in the $G_*(c)$ curve should intersect the *c*-axis at nonzero σ_a .

However “good” we might regard the data fits in Figs 6 and 7, we would not suggest that we have proved the validity of the fracture mechanics relations in Section 2. In particular, we certainly would not

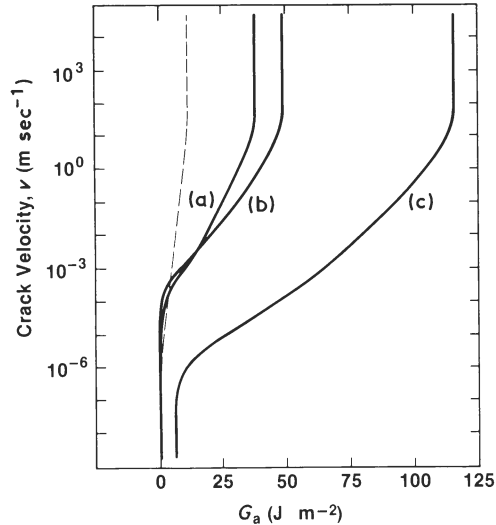


Figure 9 Apparent velocity function, v – G_a , for polycrystalline alumina in water. (– – –) Baseline zero-shielding limit ($K_r = 0 = K_\mu$), i.e. “true” crack-tip velocity function (v – G_*) from Fig. 8. (—) Nonzero shielding, Vickers indentation flaws (loads P), dynamic fatigue (constant stressing rates $\dot{\sigma}_a$): (a) $P = 3 \text{ N}$, $\dot{\sigma}_a = 10^3 \text{ MPa sec}^{-1}$; (b) $P = 30 \text{ N}$, $\dot{\sigma}_a = 10^3 \text{ MPa sec}^{-1}$; (c) $P = 30 \text{ N}$, $\dot{\sigma}_a = 10^{-1} \text{ MPa sec}^{-1}$. (Note expanded G scale relative to Fig. 8).

assert that the results confirm the fundamental correctness of the hyperbolic form of the intrinsic v – G_* function in Equation 10. Nevertheless, we may feel confident that the deconvoluted curves in Fig. 8 do faithfully represent the more important quantitative features of this intrinsic function, including the surface energy levels that define the thresholds.

In this context of velocity functions, we submit that caution needs to be exercised in the interpretation of results from conventional large-crack tests, because of the shielding effects associated with *R*-curve behaviour. In an actual experiment one monitors the applied mechanical energy release rate G_a , not the energy rate G_* experienced at the crack tip. Thus the apparent velocity relation, v – G_a , will generally differ from the intrinsic relation, v – G_* , and, moreover, will be history dependent. An important factor is the starting location along the *R*-curve; larger starting cracks will experience greater shielding, resulting in displacements of the v – G_a curves to the right on a velocity diagram. Similar displacements may be anticipated at slower loading rates. As an illustration, we show in Fig. 9 hypothetical v – G_a curves for our indentation-flaw alumina–water system, generated from our algorithm for three designated P – $\dot{\sigma}_a$ combinations. We reiterate, these are the curves that would be obtained experimentally if one were to evaluate $G_a = K_a^2/E' = \psi^2 \sigma_a^2 c/E'$ (Equations 2, 3 and 11, $K_r = 0 = K_\mu$) from direct monitoring of the applied load and the crack size. As foreshadowed, the displacements become more pronounced with increasing indentation load and decreasing stress rate. Such a history dependence could account for the reports of progressive run-to-run v – G data shifts in the literature [30–32].

Another distinguishing feature of *R*-curve behaviour is the “flaw tolerance” referred to in Sections 1 and 3.2 [24]. Again, we use the algorithm to demonstrate the point, by computing hypothetical dynamic fatigue

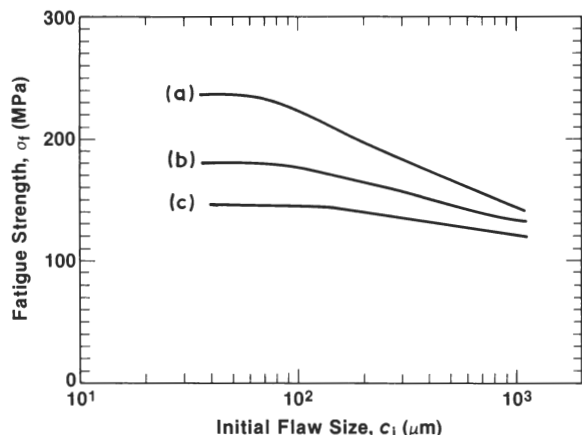


Figure 10 Plot of dynamic fatigue strength, σ_f , as function of starting size, c_i , of natural flaws ($K_r = 0$) for alumina-water system, at specified stressing rates: (a) $\dot{\sigma}_a = 10^4$ MPa sec $^{-1}$; (b) $\dot{\sigma}_a = 10^1$ MPa sec $^{-1}$; (c) $\dot{\sigma}_a = 10^{-2}$ MPa sec $^{-1}$.

strength, σ_f , against initial flaw size, c_i , at prescribed constant stressing rates for our alumina-water system. The results of such computations for natural flaws (i.e. $K_r = 0$ in Equation 3) are plotted in Fig. 10. The strength values remain relatively constant up to initial flaw sizes of several tens of micrometres. Such insensitivity is attributable to the stabilizing influence of the (negative) $K_\mu(c)$ function on the crack driving force, as reflected for instance in the strongly diminishing $G_*(c)$ function to the left of the minimum in Fig. 5.

This stabilizing influence may be demonstrated more explicitly by plotting out the complete evolutionary path to failure. It is a trivial matter to extract this path directly from the algorithm. Thus in Fig. 11 we plot three $\sigma_a(c)$ functions (solid curves) at constant $\dot{\sigma}_a$ for our dynamic fatigue, indentation-flaw ($P = 30$ N) alumina-water system (cf. Fig. 6). The final instability configurations, c_f (arrowed), in these curves occur at relatively large crack sizes (cf. initial sizes c_i , at $\sigma_a = 0$), the more so the slower the stressing rate; indeed, at the slowest rate represented the crack undergoes several hundred micrometres of precursor stable extension. For comparison, we include in Fig. 11 corresponding bounding quasi-equilibrium functions, computed using $G_* = 2\gamma_0$ (upper dashed curve) or $G_* = 2\gamma_1$ (lower dashed curve) in place of the v - G_* relations in Equation 10 as a condition for extension in the algorithm. We note the tendency for the fatigue curves at the extremes of the stressing-rate range to approach these quasi-equilibrium limits: at fast rates the failure stress approaches the inert strength, confirming that the crack spends most of its pre-failure life close to $G_* = 2\gamma_0$; conversely, at slow rates the failure stress approaches the fatigue limit, indicating a pre-failure life perpetually close to $G_* = 2\gamma_1$.

In conclusion, we have described a procedure for analysing specific fatigue (constant stress and constant stressing rate) and material-environment (alumina-water) systems. There would appear to be no restriction on the general flexibility of the algorithm. In principle, any stressing state (e.g. complex, cyclic loading), velocity function (e.g. air or other reactive environment), or even R -curve mechanism (e.g. transformation

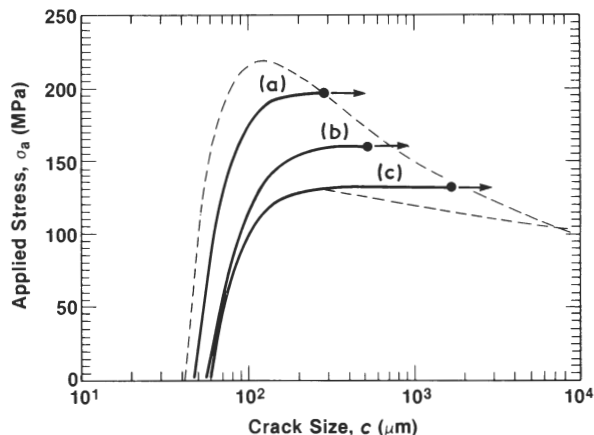


Figure 11 Plot of fatigue $\sigma_a(c)$ function for Vickers indentation flaws, $P = 30$ N, in alumina-water system, at prescribed stressing rates (—): (a) $\dot{\sigma}_a = 10^4$ MPa sec $^{-1}$; (b) $\dot{\sigma}_a = 10^1$ MPa sec $^{-1}$; (c) $\dot{\sigma}_a = 10^{-2}$ MPa sec $^{-1}$. Also included are comparative quasi-equilibrium plots for inert strength limit (upper ---) and fatigue limit (lower ---).

toughening), could be handled by suitable modifications to individual elements in the formulation.

Acknowledgements

The authors gratefully acknowledge many stimulating discussions with Y-W. Mai, S. J. Bennison and R. F. Cook on this work. Alumina specimens were kindly provided by J. D. Sibold and M. J. Readey of Coors Ceramics. Funding was provided by the (US Air Force) Office of Scientific Research.

References

1. S. M. WIEDERHORN, in "Fracture Mechanics of Ceramics", Vol. 2, edited by R. C. Bradt, D. P. H. Hasselman and F. F. Lange (Plenum, New York, 1974) p. 613.
2. A. G. EVANS and S. M. WIEDERHORN, *Int. J. Fract.* **10** (1974) 379.
3. S. M. WIEDERHORN and J. E. RITTER Jr, in "Fracture Mechanics Applied to Brittle Materials", edited by S. W. Freiman, ASTM Special Technical Publication no. 678 (ASTM, Philadelphia, Pennsylvania, 1979) p. 202.
4. H. H. JOHNSON and P. C. PARIS, *Engng Fract. Mech.* **1** (1968) 3.
5. R. F. COOK, *J. Mater. Res.* **1** (1986) 852.
6. T. A. MICHALSKE, in "Fracture Mechanics of Ceramics", Vol. 5, edited by R. C. Bradt, D. P. H. Hasselman and F. F. Lange (Plenum, New York, 1983) p. 277.
7. B. R. LAWN, D. H. ROACH and R. M. THOMSON, *J. Mater. Sci.* **22** (1987) 4036.
8. S. J. BENNISON and B. R. LAWN, *Acta Metall* in press.
9. H. HUBNER and W. JILLEK, *J. Mater. Sci.* **12** (1977) 117.
10. R. W. STEINBRECH, R. KNEHANS and W. SCHAARWACHTER, *ibid.* **18** (1983) 265.
11. R. F. COOK, B. R. LAWN and C. J. FAIRBANKS, *J. Amer. Ceram. Soc.* **68** (1985) 604.
12. C. J. FAIRBANKS, B. R. LAWN, R. F. COOK and Y-W. MAI, in "Fracture Mechanics of Ceramics", Vol. 8, edited by R. R. Bradt, A. G. Evans, D. P. H. Hasselman and F. F. Lange (Plenum, New York, 1986) p. 23.
13. P. L. SWANSON, C. J. FAIRBANKS, B. R. LAWN, Y. W. MAI and B. J. HOCKEY, *J. Amer. Ceram. Soc.* **70** (1987) 279.
14. Y-W. MAI and B. R. LAWN, *ibid.* **70** (1987) 289.
15. R. F. COOK, C. J. FAIRBANKS, B. R. LAWN and Y-W. MAI, *J. Mater. Res.* **2** (1987) 345.

16. M. SAKAI and R. C. BRADT, *J. Ceram. Soc. Jpn* **96** (1988) 801.
17. B. R. LAWN, *J. Amer. Ceram. Soc.* **66** (1983) 83.
18. P. F. BECHER, T. N. TIEGS, J. C. OGLE and W. H. WARWICK, in "Fracture Mechanics of Ceramics", Vol. 7, edited by R. C. Bradt, A. G. Evans, D. P. H. Hasselman and F. F. Lange (Plenum, New York, 1986) pp. 61-73.
19. D. B. MARSHALL and B. R. LAWN, *J. Amer. Ceram. Soc.* **63** (1980) 532.
20. P. CHANTIKUL, B. R. LAWN and D. B. MARSHALL, *ibid.* **64** (1981) 322.
21. B. R. LAWN, D. B. MARSHALL, G. R. ANSTIS and T. P. DABBS, *J. Mater. Sci.* **16** (1981) 2846.
22. E. R. FULLER, B. R. LAWN and R. F. COOK, *J. Amer. Ceram. Soc.* **66** (1983) 314.
23. R. F. COOK, B. R. LAWN and C. J. FAIRBANKS, *ibid.* **68** (1985) 616.
24. S. J. BENNISON and B. R. LAWN, *J. Mater. Sci.*, in press.
25. B. R. LAWN and T. R. WILSHAW, "Fracture of Brittle Solids" (Cambridge University Press, London, 1975) Chs 3, 8.
26. B. R. LAWN, *J. Mater. Sci.* **10** (1975) 469.
27. B. R. LAWN and S. LATHABAI, *Mater. Forum* **11** (1988) 313.
28. D. B. MARSHALL and B. R. LAWN, *J. Mater. Sci.* **14** (1979) 2001.
29. Y-W. MAI and B. R. LAWN, *Ann. Rev. Mater. Sci.* **16** (1986) 415.
30. S. W. FREIMAN, K. R. MCKINNEY and H. L. SMITH, in "Fracture Mechanics of Ceramics", Vol. 2, edited by R. C. Bradt, D. P. H. Hasselman and F. F. Lange (Plenum, New York, 1974) p. 659.
31. B. J. PLETKA and S. M. WIEDERHORN, *J. Mater. Sci.* **17** (1982) 1247.
32. P. L. SWANSON, in "Fracture Mechanics of Ceramics", Vol. 8, edited by R. C. Bradt, A. G. Evans, D. P. H. Hasselman and F. F. Lange (Plenum, New York, 1986) p. 299.

*Received 27 January
and accepted 13 February 1989*